Journal of Energy Chemistry 97 (2024) 444–452

Contents lists available at ScienceDirect

Journal of Energy Chemistry

journal homepage: www.elsevier.com/locate/jechem

http://www.journals.elsevier.com/journal-of-energy-chemistry/

Surface engineering of P2-type cathode material targeting long-cycling and high-rate sodium-ion batteries

Jun Xiao [a,b], Yang Xiao [b], Shijian Wang [a], Zefu Huang [a], Jiayi Li [b], Cheng Gong [b], Guilai Zhang [b], Bing Sun [a], Hong Gao [b,*], Huiqiao Li [c], Xin Guo [a], Yong Wang [b], Hao Liu [a,*], Guoxiu Wang [a,*]

[a] Centre for Clean Energy Technology, School of Mathematical and Physical Sciences, Faculty of Science, University of Technology Sydney, Broadway, Sydney, New South Wales 2007, Australia
[b] Joint International Laboratory on Environmental and Energy Frontier Materials, School of Environmental and Chemical Engineering, Shanghai University, Shanghai 200444, China
[c] State Key Laboratory of Materials Processing and Die and Mould Technology, School of Materials Science and Engineering, Huazhong University of Science and Technology, Wuhan 430074, Hubei, China

ARTICLE INFO

Article history:
Received 26 May 2024
Revised 5 June 2024
Accepted 5 June 2024
Available online 14 June 2024

Keywords:
Layered metal oxides
Sodium-ion batteries
P2-type structure
Surface engineering

ABSTRACT

The widespread interest in layered P2-type Mn-based cathode materials for sodium-ion batteries (SIBs) stems from their cost-effectiveness and abundant resources. However, the inferior cycle stability and mediocre rate performance impede their further development in practical applications. Herein, we devised a wet chemical precipitation method to deposit an amorphous aluminum phosphate ($AlPO_4$, denoted as AP) protective layer onto the surface of P2-type $Na_{0.55}Ni_{0.1}Co_{0.1}Mn_{0.8}O_2$ (NCM@AP). The resulting NCM@5AP electrode, with a 5 wt% coating, exhibits extended cycle life (capacity retention of 78.4% after 200 cycles at 100 mA g^{-1}) and superior rate performance (98 mA h g^{-1} at 500 mA g^{-1}) compared to pristine NCM. Moreover, our investigation provides comprehensive insights into the phase stability and active Na^+ ion kinetics in the NCM@5AP composite electrode, shedding light on the underlying mechanisms responsible for the enhanced performance observed in the coated electrode.

1. Introduction

The development and commercial utilization of sodium-ion batteries (SIBs) critically depend on the identification of suitable cathode materials [1–6]. Among the diverse range of investigated cathode materials, layered metal oxides Na_xTMO_2 (TM = transition metals, including Mn, Ni, Fe, etc.) have gained considerable attention due to their favorable attributes, including high specific capacity, operating voltage, and energy density [7–13]. Generally, these layered Na_xTMO_2 electrode materials adopt P2- or O3-type structures, where Na^+ ions reside in either prismatic or octahedral central sites within the crystal structure [14–18]. P2-type cathodes, which offer direct migration pathways, demonstrate superior rate performance and excellent cycle stability. In contrast, O3-type cathodes, despite having sufficient Na^+ content, exhibit sluggish kinetics, complex phase transitions, and increased sensitivity to moisture [19–24]. As a result, extensive research has focused on P2-type materials, especially Mn-based layered metal oxides, which have the advantages of low cost and environmental-friendliness. Nevertheless, the P2-type Mn-based materials suffer from the detrimental P2-O2 or P2-OP4 phase transition when operated at cut-off voltage above 4.2 V. These transitions lead to significant volume changes and fast capacity decay. Additionally, the presence of Mn^{3+} ions induces the Jahn-Teller effect, further accelerating the degradation of the host structure and adversely affecting the electrochemical properties [25–30].

To date, multifarious strategies have been proposed to address the aforementioned issues. Inactive elements (Li, Zn, Cu, Ti, etc.) doping in the Na layers or TMO_2 layers can greatly meliorate the structural stability and prolong the cycle life [31–36]. Biphasic structures (P2/O3, P2/P3, and P3/O3) can effectively combine the advantages of each phase and generate a synergistic effect, so these composite materials can achieve distinguished electrochemical properties [37–41]. Besides, surface coating is a straightforward and valid maneuver to minimize the capacity fade and maintain the original structure. The protective layer can suppress the gliding of the TMO_2 layers and refrain the Jahn-Teller effect of Mn^{3+} during

* Corresponding authors.
E-mail addresses: hgao1122@shu.edu.cn (H. Gao), hao.liu@uts.edu.au (H. Liu), Guoxiu.Wang@uts.edu.au (G. Wang).

https://doi.org/10.1016/j.jechem.2024.06.007

repetitious sodiation/desodiation process [42–45]. For instance, Jo et al. coated the typical P2-type $Na_{2/3}Ni_{1/3}Mn_{2/3}O_2$ cathode with bioinspired β-$NaCaPO_4$ nanolayer, effectively obliterating the HF and H_2O originated from electrolyte decomposition [42]. Deng et al. demonstrated that incorporating a $NaTi_2(PO_4)_3$ layer on the surface of $Na_{0.65}[Mn_{0.70}Ni_{0.16}Co_{0.14}]O_2$ greatly restrains the adverse P2-O2 phase transition and ameliorates structural reversibility, thereby, the as-prepared electrode maintained 84.3% of its initial capacity even at 5 C after 500 cycles [45].

$AlPO_4$ (AP), with the merit of low-cost, is a widely explored prospective coating material in lithium-ion batteries (LIBs), however, its investigation, especially the detailed working mechanism in SIBs, has been hardly reported. In addition, nickel can increase the working potential of the Mn-based layered metal oxides, while cobalt can stabilize the layered structure and enhance the rate performance [27,45]. Herein, we prepared a P2-type $Na_{0.55}Ni_{0.1}Co_{0.1}Mn_{0.8}O_2$ (NCM) cathode material via a simple solid-state reaction, followed by a wet chemical reaction to coat a AP protective layer. The coating can effectively mitigate the Jahn-Teller effect of Mn^{3+} by reducing the amount of Mn^{3+} ions. The introduction of a 5 wt % AP coating on the NCM cathode (NCM@5AP) behaves a significant improvement in Na^+ kinetics and cycling stability compared to pristine NCM. Specifically, the optimized NCM@5AP electrode delivers a specific capacity of 98 mA h g^{-1} at a high current density of 500 mA g^{-1}. Moreover, it showcased excellent capacity retention of 78.4% after 200 cycles at 100 mA g^{-1}. To elucidate the factors contributing to the enhanced electrochemical performance, we conducted rigorous investigations. In-situ X-ray diffraction (XRD) analysis unveils the single-phase reaction mechanism of the NCM@5AP electrode, corroborating its exceptional structural stability during the sodiation/desodiation process. Complementarily, density functional theory (DFT) simulations showcase a lower diffusion barrier energy for NCM@5AP compared to pristine NCM, offering additional evidence of how surface modification facilitates the accelerated diffusion rate of Na^+ ions. These comprehensive findings shed light on the mechanisms underpinning the improved performance of the coated electrode.

2. Experimental

2.1. Material synthesis

P2-type $Na_{0.55}Ni_{0.1}Co_{0.1}Mn_{0.8}O_2$ (NCM) was prepared by a facile solid-state reaction. Firstly, an appropriate amount of Na_2CO_3 (Sinopharm, >99%), $Mn(CH_3COO)_2{\cdot}4H_2O$ (Sinopharm, >99%), $Co(CH_3COO)_2{\cdot}4H_2O$ (Sinopharm, ≥99.5%), and $Ni(CH_3COO)_2{\cdot}4H_2O$ (Sinopharm, ≥98%) were manually mixed in an agate mortar according to the metal ratios. Then, the resulting powders were treated at 450 °C for 5 h in air atmosphere and slowly cooled to room temperature. Hereafter, the obtained dry powder was pressed into pellets under 10 MPa and calcined at 500 °C for 3 h followed by 900 °C for 12 h in air.

The $AlPO_4$ (AP) coating process was realized by a wet chemical precipitation reaction. Stoichiometric amounts of $Al_2(SO_4)_3{\cdot}18H_2O$ (Sinopharm, ≥99%) and $NH_4H_2PO_4$ (Sinopharm, ≥99%) were added to a mixture solution, which was composed of 16 mL distilled water and 32 mL absolute ethyl alcohol under a vigorous stir to form a suspension. Then the pristine NCM powders were added into the above solution and stirred at 80 °C to evaporate the solvent. Finally, the obtained powders were calcinated at 400 °C for 5 h in air to obtain the NCM@AP composites. Different amount of AP was designed (3, 5, and 7 wt%) to get the corresponding NCM@AP composites labelled as NCM@3AP, NCM@5AP, and NCM@7AP.

2.2. Material characterizations

The morphological and microstructural details were analyzed by the high-resolution transmission electron microscope (HR-TEM, JEOL-2100F) and scanning electron microscope (SEM, SU5000). Element distribution was conducted on TEM-energy dispersive spectroscopy (EDS). Crystal structure properties were scrutinized by X-ray diffraction (XRD, Rigaku D/MAX 2200VPC) using Cu K_a radiation in the 2θ range from 10° to 80°. The X-ray photoelectron spectroscopy (XPS, ESCALAB 250 Xi) was employed to study the valence state of the elements. Inductively coupled plasma optical emission spectrometry (ICP-OES, Optima 2100DV) was applied to determine the ratio of different atoms. The Fourier transform infrared (FTIR) spectroscopy tests were performed on BIO-RAD FTS 135 spectrometer. And the raman spectroscopy measurement was performed on Thermo Fischer DXR. In addition, the in-situ XRD patterns of NCM@5AP electrode were collected via Swagelok cell within 1.5–4.3 V at 50 mA g^{-1}.

2.3. Electrochemical measurements

The coin cells (CR2032-type) were assembled in an argon-filled glove box with cathode electrode composed of 70 wt% active material, 20 wt% acetylene black, and 10 wt% polyvinylidene fluoride (PVDF). The loading amount of active materials in the electrode obtained by vacuum drying at 80 °C overnight was about 1.2 mg cm^{-2}. Sodium metal and glass fiber (GF/D) were used as counter electrode and separator. The electrolyte was consisted of 1 M $NaClO_4$ dissolved in ethylene carbonate (EC) and diethyl carbonate (DEC) (1:1 by volume) with 5% fluoroethylene carbonate (FEC) as addictive. Neware CT-4008 battery test system was employed to test the charge and discharge performance within the voltage range of 1.5–4.3 V (vs. Na^+/Na). Cyclic voltammetry (CV) measurements and electrochemical impedance spectroscopy (EIS, 100 kHz–10 mHz) tests were conducted on CHI660 electrochemical workstation. The pre-sodiated commercial hard carbon was well matched with NCM@5AP (1: 1.4 by molar ratio) to assemble full battery at the voltage range of 2.0–4.2 V.

2.4. DFT calculation

Spin-polarized first-principle calculations were performed by the DFT using the Vienna Ab-initio Simulation Package (VASP) package. The generalized gradient approximation (GGA) with the Perdew-Burke-Ernzerhof (PBE) functional were used to describe the electronic exchange and correlation effects. Only G point and Methfessel-Paxton electronic smearing were adopted for the integration in the Brillouin zone for geometric optimization. The simulation was run with a cutoff energy of 500 eV throughout the computations. These settings ensure convergence of the total energies to within 1 meV per atom. Structure relaxation proceeded until all forces on atoms were less than 10 meV $Å^{-1}$ and the total stress tensor was within 0.05 GPa of the target value. The energy barrier for water splitting energy barrier was calculated using the nudged elastic band (NEB) method. The calculation parameters and convergence criteria were kept the same as in the ground state calculations.

3. Results and discussion

The preparation process of the pristine $Na_{0.55}Ni_{0.1}Co_{0.1}Mn_{0.8}O_2$ (NCM) and the NCM@AP composite with different AP contents is illustrated in Fig. 1(a). Specifically, the pristine NCM is synthesized by a solid-state reaction process with two step calcination procedures. A wet chemistry method is employed to deposit AP

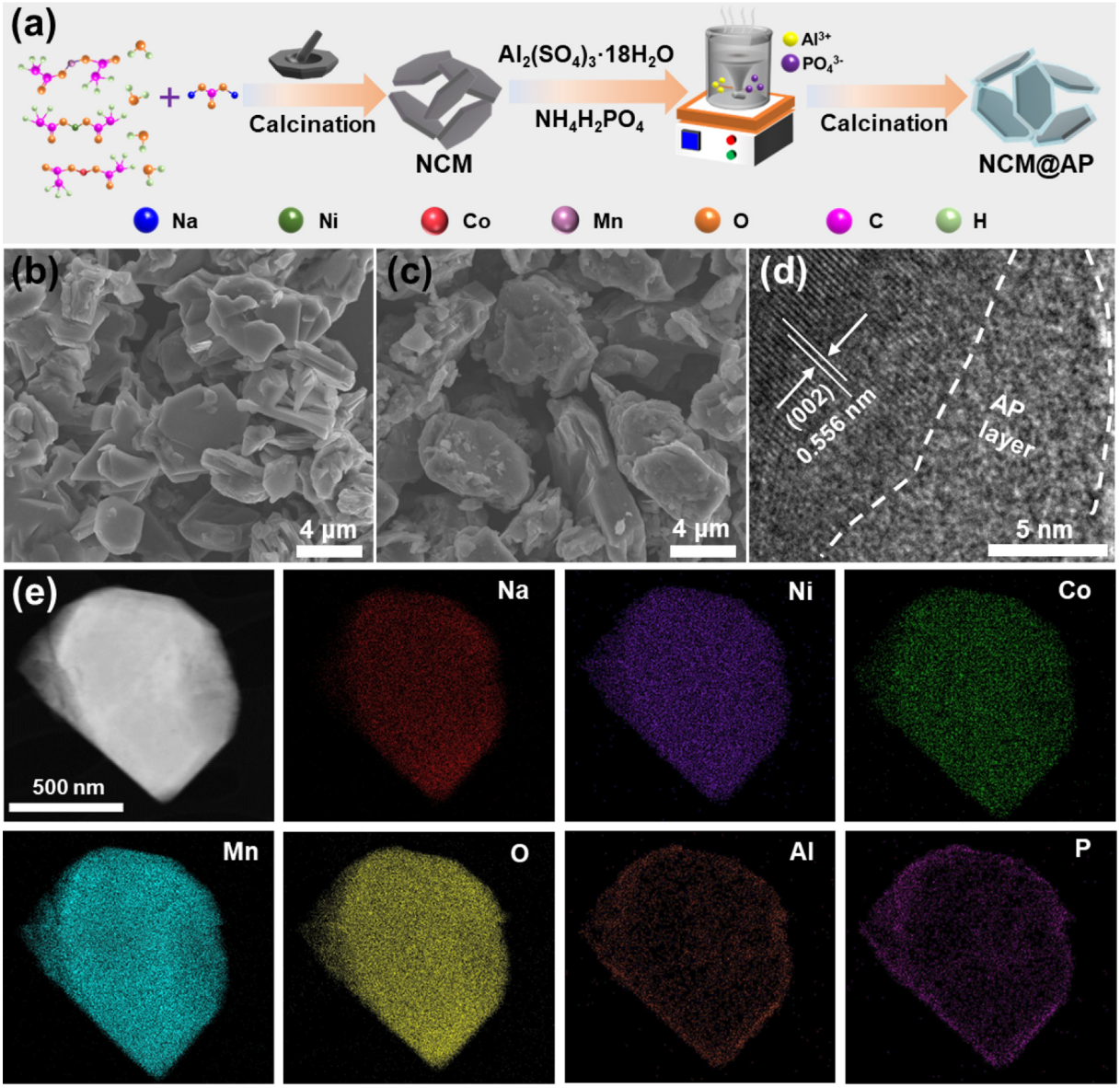

Fig. 1. (a) Schematic diagram of the preparation process for NCM@AP. (b, c) SEM images of NCM and NCM@5AP. (d) HR-TEM image of NCM@5AP. (e) STEM and corresponding elemental mapping images of NCM@5AP.

protective layer on the surface of pristine NCM. For comparison, these composites with different AP amount (3, 5, and 7 wt%) are denoted as NCM@3AP, NCM@5AP, and NCM@7AP. The surface morphologies of the pristine NCM and AP-coated cathode materials were characterized by SEM (Fig. 1b, c and Fig. S1). And all of the four samples exhibit plate-like shapes with diameters ranging from 2 to 10 μm, indicating that the surface-treated process has no influence on the particle size. And the pristine NCM displays smooth surface, whereas some smaller nanoparticles are observed on the surface of other three surface-modified products, which might be attributed to the AP coating modification. Moreover, the surface becomes rougher as the amount of AP increases and the element composition of pristine NCM is confirmed by elemental mapping images (Fig. S2). The detailed crystal structure information of pristine NCM and NCM@5AP was characterized by high-resolution TEM (HR-TEM). To be more specific, the adjacent lattice fringes with an interplanar distance of 0.275 nm in pristine NCM belongs to the (004) planes of hexagonal layered structure (Fig. S3). While for the NCM@5AP, a lattice width featuring 0.556 nm is found in Fig. 1(d), which corresponds to the d-spacing values of typical (002) planes of P2-type material. Meanwhile, an obvious amorphous coating layer with a thickness of about 10 nm can be observed. Moreover, EDS mapping images manifest uniform distribution of Na, Ni, Co, Mn, O, Al, and P elements in NCM@5AP (Fig. 1e).

Fig. 2(a) demonstrates the XRD patterns of the pristine NCM and surface-modified NCM@3AP, NCM@5AP, and NCM@7AP materials. Clearly, all the samples exhibit similar diffraction peaks belonging to a hexagonal $P6_3/mmc$ space group (JPCDS:54-0894) without any impurities, suggesting that AP surface engineering has no effect on the layered structure character of pristine NCM [46,47]. The (002) peak located at about 16° consecutively shifts to low degree along with the increased AP content, indicating the enlargement of *c*-axis. On the contrary, three peaks between 36°–44° experience a converse tendency, suggesting the shrinking of parameter a (Fig. S4). All the results illustrate that a few AP incorporates into the host structure of pristine NCM, thus cause trifling changes in lattice parameters. Correspondingly, rietveld refine-

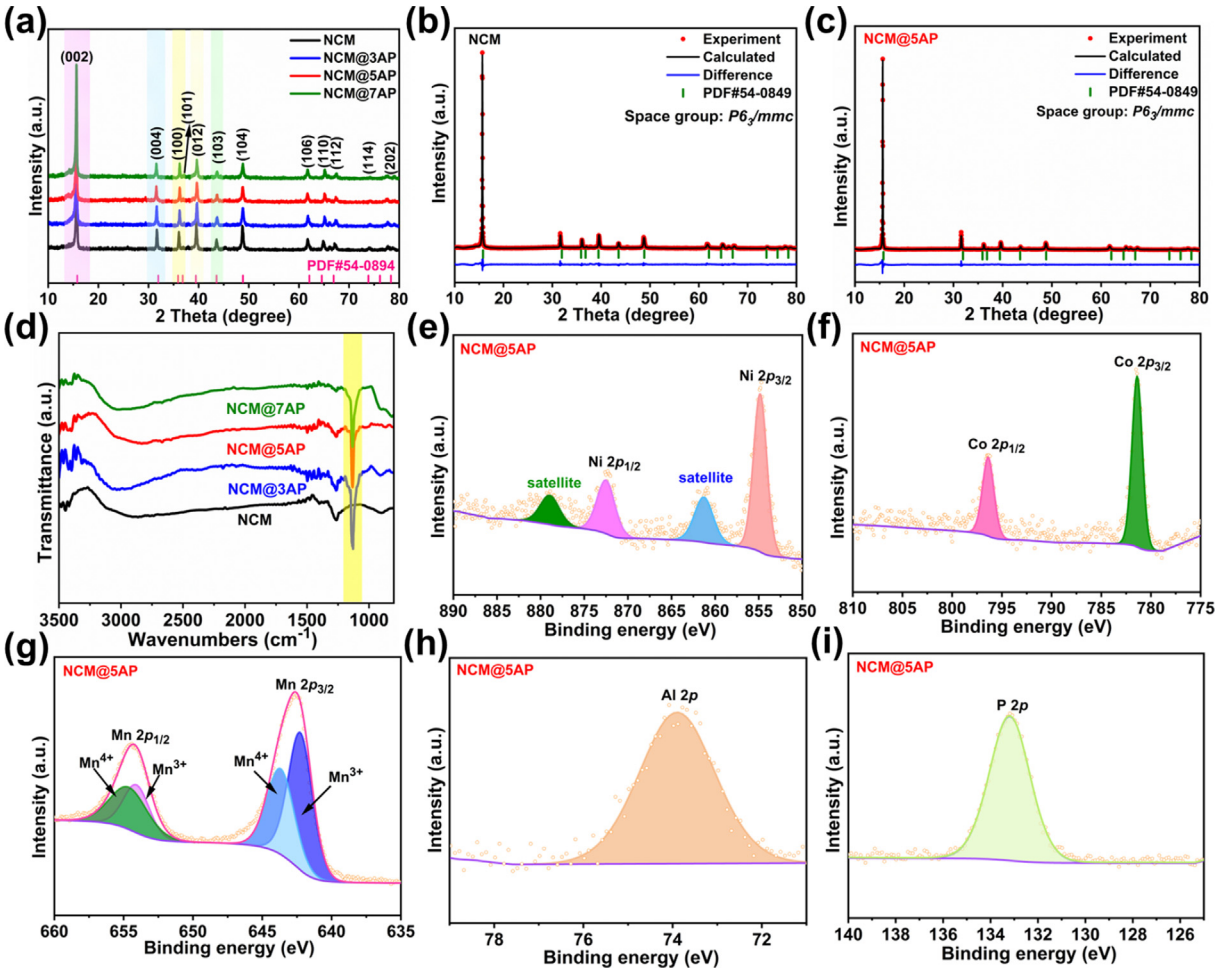

Fig. 2. (a) XRD profiles of pristine NCM, NCM@3AP, NCM@5AP, and NCM@7AP. (b, c) The Rietveld refinement profiles of pristine NCM and NCM@5AP. (d) The Fourier transform infrared (FT-IR) spectrum of as-prepared electrodes. High-resolution spectra of (e) Ni 2*p*, (f) Co 2*p*, (g) Mn 2*p*, (h) Al 2*p*, and (i) P 2*p* of NCM@5AP.

ment method is further used to collect the detailed structural data (Fig. 2b, c and Fig. S5) and the crystal parameters are summarized in Table S1. It is worth noting that the TMO_2 layer thickness decreases whereas the d-spacing of the Na^+ diffusion layer aggrandizes as the increased AP. This result further confirms the incorporation of part AP into the bulk structure and thus accelerates the Na^+ ions diffusion kinetics. The corresponding crystal structures of pristine NCM and NCM@5AP are depicted in Fig. S6. Additionally, AP might be amorphous because no diffraction peak for AP is observed in these coated cathode materials [43,45].

In order to confirm the above speculation, FT-IR measurement was carried out to investigate the existence of AP. As presented in Fig. 2(d), the absorption band in the region of 1000–1200 cm^{-1} is attributed to typical antisymmetric stretching modes of PO_4^{3-}, corroborating the successful AP coating on NCM@3AP, NCM@5AP, and NCM@7AP [43]. In the Raman spectroscopy, both two samples behave similar intense bands at around 592 (A_{1g}) and 493 (E_g) cm^{-1}, which ascribe to unsymmetrical stretching vibration of TM–O bond and bending vibration of O–TM–O bond, respectively (Fig. S7). However, the A_{1g} value of NCM@5AP presents a small shift, indicating alterant local interatomic distance after coating, which further comfirms that partial AP has been doped into the crystal structure of pristine NCM [8]. Moreover, the molar ratios of the constituent elements in these composites detected by ICP-OES are in good agreement with the anticipated values (Table S2). Besides, the XPS analysis was used to investigate the valent states of composition elements. Full spectrum reveals that Na, Ni, Co, Mn, O, Al, and P can be clearly detected in NCM@5AP while the last two components could not be found in pristine NCM (Fig. S8). All of the four samples' binding energy peaks of Ni 2*p* spectrum located at 854.7 and 872.3 eV corresponding to Ni $2p_{3/2}$ and Ni $2p_{1/2}$, indicating the existence of Ni^{2+} (Fig. 2e and Fig. S9) [40,48,49]. And in the high-resolution spectrum of Co 2*p*, the Co $2p_{3/2}$, and Co $2p_{1/2}$ positions at 781.5 and 796.1 eV manifest the existence of trivalent cobalt in all products (Fig. 2f and Fig. S10) [40,50]. The Mn 2*p* core-level spectra show four similar peaks, demonstrating that Mn^{3+} (642.3, 654.2 eV) and Mn^{4+} (643.8, 655.1 eV) coexist in these materials (Fig. 2g and Fig. S11) [48,51,52]. However, the ratio of Mn^{3+}/Mn^{4+} is decreased when increasing the AP amount, as summarized in Table S3, which caused by the insertion of partial Al^{3+} into the bulk structure of pristine cathode. The structural distortion and collapse originated from the Jahn-Teller effect of Mn^{3+} is prevailing in the Mn-based cathodes for SIBs, hence reduced Mn^{3+} content by coating layer can effectively contribute to preeminent structural stability and cycle life. Furthermore, as displayed in Fig. 2(h and i), the binding energy peaks at 74 and 133.2 eV are assigned to Al 2*p* and P 2*p*, which are not detected in pristine NCM, suggesting the AP is triumphantly covered on the surface of NCM@5AP [43,44]. And the corresponding in-depth spectra further substantiate partial AP has entered into the host structure (Fig. S12). All the aforementioned measurements authenticate that pristine NCM and AP-coated electrode materials are successfully synthesized through a solid-state reaction and chemical coprecipitation method.

To assess the impact of AP coating on electrochemical performance, the prepared sample served as the positive electrode material in a half-cell configuration. Metal sodium was used as the counter electrode, and the testing was carried out in the voltage window of 1.5–4.3 V. Fig. 3(a) and Fig. S13(a–c) illustrate the CV profiles of the as-prepared cathodes at a scan rate of 0.1 mV s^{-1} during the initial five cycles. For the pristine NCM, the redox peaks below 3.0 V (vs. Na^+/Na) are ascribed to Mn^{3+}/Mn^{4+} couple, and the minor peaks between 3.0 and 4.0 V are related to reversible redox reaction of Ni^{2+}/Ni^{3+} and Ni^{3+}/Ni^{4+} couples, respectively [40,49]. More impressively, the peak pair at 4.20/4.05 V within high voltage range may be associated with the adverse phase transition [34,53]. In addition, the curves of NCM@3AP, NCM@5AP, and NCM@7AP exhibit similar peak shape to pristine NCM, except for the redox couples belonging to the detrimental phase transition. In the meantime, the profiles of these AP-coated samples with highly overlapping character indicate better reversibility than the pristine NCM. This phenomenon effectually confirms that the protective coating layer is conducive to ameliorating the structural stability of the pristine electrode material and restraining pernicious phase evolution.

Correspondingly, the selected charge/discharge curves of the four electrode materials cycled at 20 mA g^{-1} within 1.5–4.3 V are presented in Fig. 3(b) and Fig. S13(d–f). All the plateaus and several slopes observed in the profiles are coincided closely with the CV results. The discharge capacities of pristine NCM, NCM@3AP, NCM@5AP, and NCM@7AP electrodes in the first cycle are 179, 163, 160, and 154 mA h g^{-1}, respectively. It is apparent that the AP-coated electrode materials deliver lower capacity than the pristine NCM, which may be caused by the dissolution of partial Na^+ during chemical precipitation process and the electrochemical inactivity of the protective layer. Nevertheless, these coated products behave better capacity retention than the pristine NCM, manifesting meliorative structural stability during sodiation/desodiation process.

Moreover, the rate capacities of these as-prepared cathode materials tested at various current densities varying from 20 to 500 mA g^{-1} are presented Fig. 3(c) and Fig. S14(a). The pristine NCM electrode delivers reversible discharge capacities of 174, 136, 108, 83, and 49 mA h g^{-1} when cycled at 20, 50, 100, 200, and 500 mA g^{-1}, respectively. And when the current density returns to 20 mA g^{-1}, only a capacity of 131 mA h g^{-1} can be recovered, indicating poor rate performance and fragile crystal structure. In contrast, the NCM@5AP electrode can achieve a discharge capacity of 98 mA h g^{-1} at the high rate of 500 mA g^{-1}, corresponding to 62.6% of its initial capacity. Surprisingly, this electrode exhibits negligible capacity fading as the current density restores to initial low rate, which is better than that of NCM@3AP and NCM@7AP. Through the selected charge/discharge curves at different rate, it is obvious that the NCM@5AP electrode exhibits more sluggish capacity fading than other three products (Fig. 3d and Fig. S14b–d). Furthermore, the NCM@5AP electrode delivers a capacity retention of 78.4% after 200 cycles at 100 mA g^{-1}. While for pristine NCM, NCM@3AP, and NCM@7AP, the retention rate is just 46.2%, 67.0%, and 65.9%, respectively (Fig. 3e and Fig. S14e). Apparently, the NCM@5AP demonstrates the best performance because 5 wt%

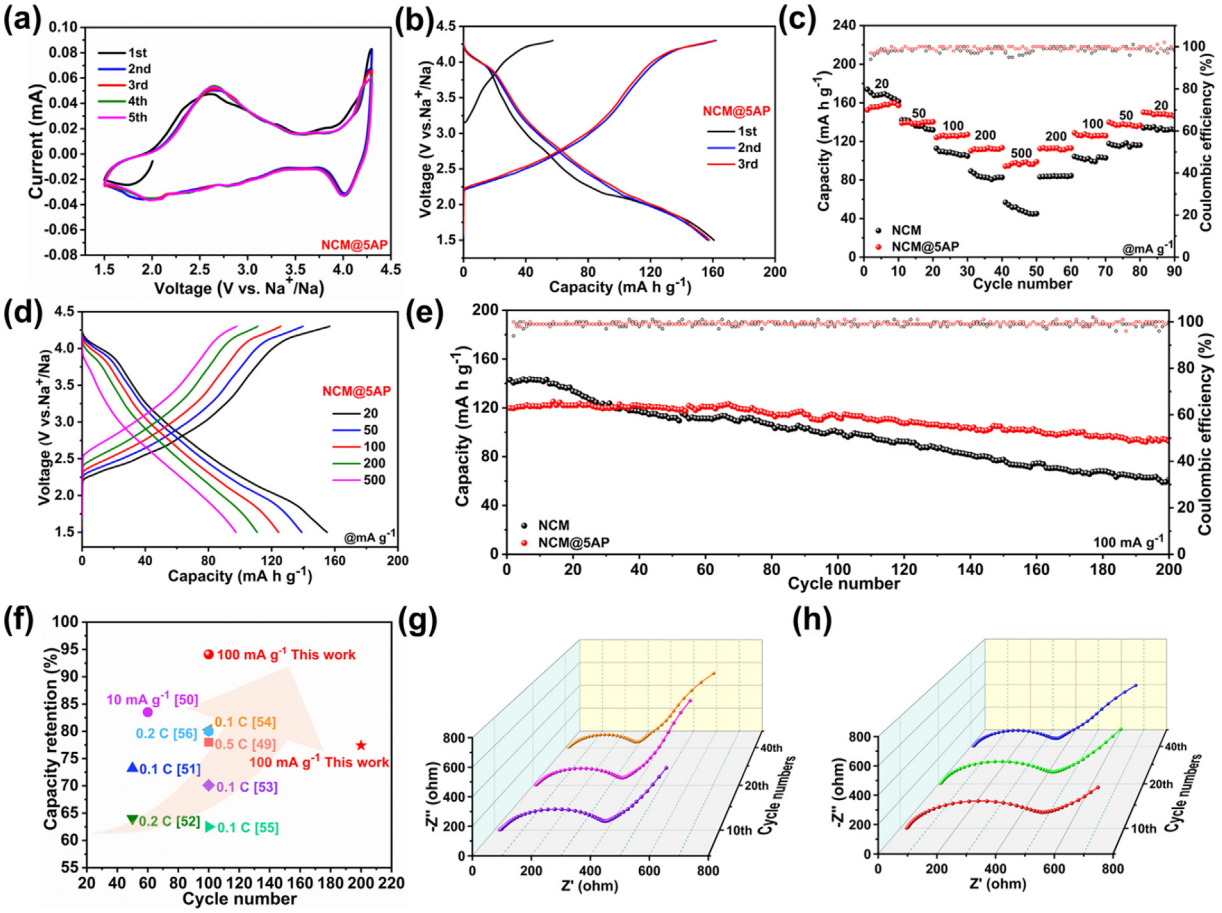

Fig. 3. (a) CV curves of NCM@5AP. (b) Charge-discharge profiles of NCM@5AP. (c) Rate capability of pristine NCM and NCM@5AP. (d) Galvanostatic charge/discharge profiles of NCM@5AP at different rate. (e) Long-term cycling life of pristine NCM and NCM@5AP at 100 mA g^{-1}. (f) Comparison of capacity retention between NCM@5AP and previous reported electrodes. (g, h) Nyquist plots of the NCM@5AP and pristine NCM at 10th, 20th, and 40th cycles.

AP can cover the surface well to enhance stability and restrain the unfavorable phase transition whereas 3 wt% AP might be not enough to defend the host structure. Increasing the amount to 7 wt% would facilitate the agglomeration of the AP particles, giving rise to inhomogeneous coating layer [43]. Furthermore, the capacity retention of NCM@5AP surpasses that of many previously reported layered cathodes, as plotted in Fig. 3(f) [54–61]. The observed data corroborate that the AP layer greatly enhance the rate performance and cycling stability, which may be attributed to the following merits: Firstly, the incorporation of partial AP into the bulk structure can enlarge the d-spacing of the Na^+ diffusion layer and *c*-axis parameters, accelerating the Na^+ transfer kinetic. Secondly, the AP layer reduces the ratio of Mn^{3+}/Mn^{4+} in the pristine NCM, thus mitigating the Jahn-Teller effect of Mn^{3+} and pernicious phase evolution. Lastly, the protective layer on the surface can inhibit the parasite reaction between the active material and electrolyte, contributing to the prolonged cycle life.

The EIS measurement is carried out to assess the impact of surface modification on the electrochemical performance. NCM@5AP provides the smallest charge transfer resistance (R_{ct}) value (385 Ω) than other electrodes before cycling (Fig. S15), and it exhibits lower resistance than pristine NCM after different cycles (Fig. 3g and h), thus NCM@5AP behaves the best rate properties. Galvanostatic intermittent titration technique (GITT) was performed to get a deep understanding of the improved Na^+ diffusion coefficients, and corresponding values were calculated using Eq. (S1) [44,47]. The typical charge/discharge curves of NCM@5AP and pristine NCM in the second cycle are plotted in Fig. 4(a) and Fig. S16(a), in which the half-cells undergo uninterrupted charging or discharging process for 15 min at a constant current (50 mA g^{-1}) and then a relaxation time for 15 min to equilibrate the voltage. As displayed in Fig. 4(b) and Fig. S16(b), the calculated average D^+_{Na} value of NCM@5AP (3.305 × 10^{-11} cm^2 s^{-1}) is larger than that of pristine NCM (2.138 × 10^{-11} cm^2 s^{-1}), which is in good agreement with the enhanced rate performance, further authenticates that the AP coating layer can accelerate migration kinetics of Na^+. CV test with diverse scan rates varying from 0.2 to 1.0 mV s^{-1} was performed on NCM@5AP and pristine NCM to analyze sodium storage mechanism (Fig. 4c and Fig. S17a). It is apparent that the redox currents aggrandize tremendously as the scan rate

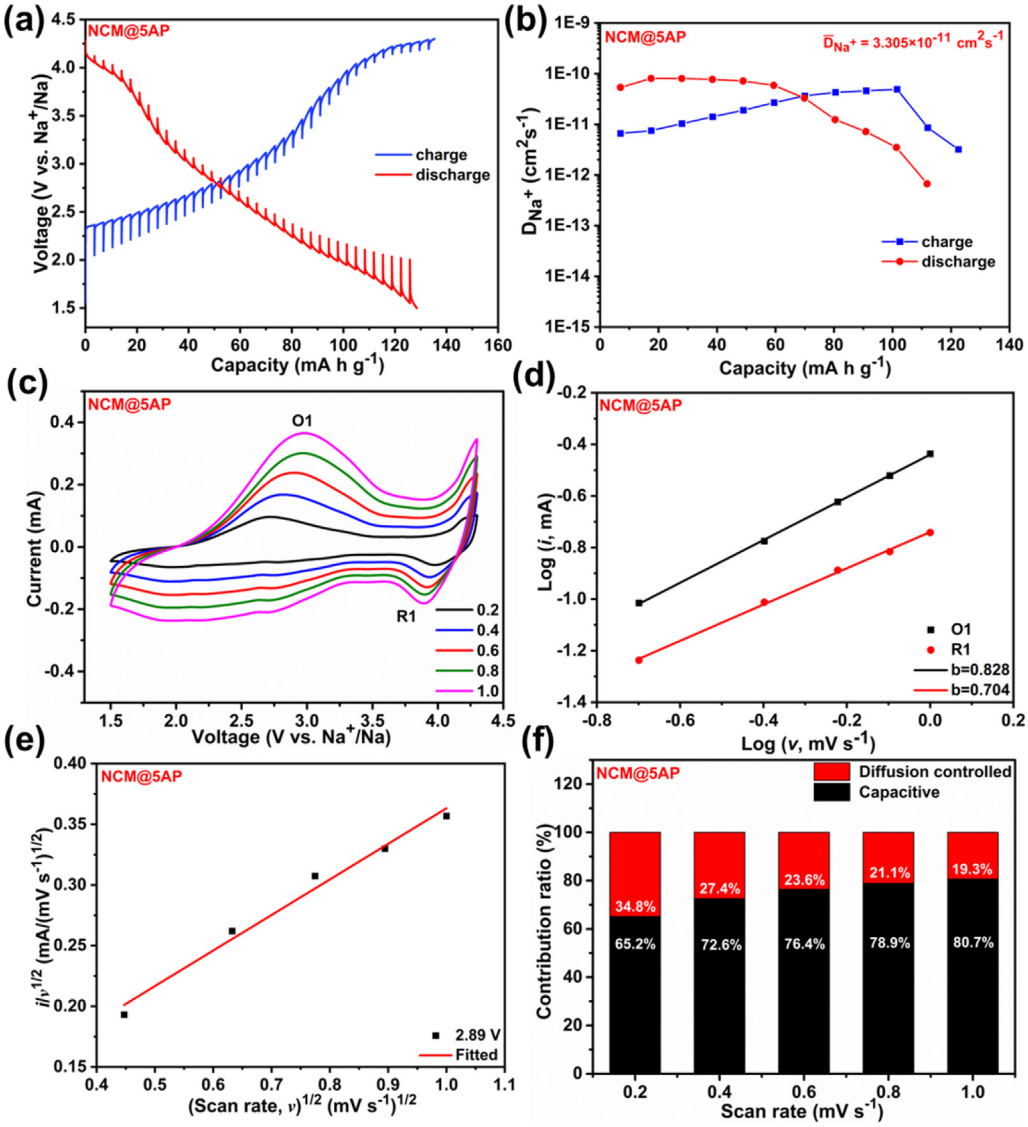

Fig. 4. (a) Charge-discharge GITT profiles of the NCM@5AP cathode at 50 mA g^{-1}. (b) The corresponding Na^+ diffusion coefficients (D^+_{Na}) of NCM@5AP cathode. (c) CV curves of the NCM@5AP electrode at different scan rates ranging from 0.2 to 1.0 mV s^{-1}. (d) Linear relationship of peak currents log(*i*) versus log(*v*) and the corresponding linear fits. (e) Linear relationship of $v^{1/2}$ versus $i/v^{1/2}$ and corresponding linear fits. (f) Contribution ratio of capacitive and diffusion-controlled behaviors at different scan rates.

increasing. Nevertheless, the profiles of NCM@5AP behave better consistency than that of the pristine NCM, reflecting ameliorative reversibility after surface modification. Meantime, faradaic intercalation or surface-controlled adsorption (pseudo-capacitance), as a dominant role during the electrochemical process, can be determined by the Eqs. ((S2) and (S3)). When the value of *b* approaches 1, it means a capacitance-controlled reaction, on the contrary, when the b value is on the verge of 0.5, the process relies on diffusion-governed behavior [49,62]. Therefore, as displayed in Fig. 4(d), the obtained b values of O1 and R1 peaks are 0.828 and 0.704 for NCM@5AP, while in the pristine NCM, the *b* value of the O1 peak is 0.890 (Fig. S17b). This behavior indicates that the Na^+ intercalation/de-intercalation process is dominated by pseudo-capacitance and AP coating layer may promote ion diffusion to some extent. Moreover, the proportion of capacitance contribution can be calculated by the Eq. (S5) [63]. Fig. 4(e) and Fig. S17(c) depict the linear relationship among $v^{1/2}$ and $i/v^{1/2}$, which can be carried out to obtain constant k_1 and k_2. Thus, as revealed in Fig. 4(f), the corresponding capacitance contribution percentage in the NCM@5AP augments from 65.2% to 80.7% with the scan rate ranging from 0.2 to 1.0 mV s^{-1}, a little lower than that of the pristine NCM at the same measurement condition (70.0% to 83.9%, Fig. S17d). It comes to the fact that the protective coating layer can facilitate the diffusion of Na^+ and achieve better electrochemical performance.

In order to unravel the working mechanism and crystal structure evolution of P2-type NCM@5AP electrode during sodiation/de-sodiation process, we performed in-situ XRD measurement between 1.5 and 4.3 V at 50 mA g^{-1} with Al foil as current collector. The corresponding intensity contour maps and voltage curves during initial charge/discharge process are presented in Fig. 5(a). It is distinct that this cathode material maintains the P2-type structure well throughout the testing procedure without appearance of new peaks for other phase, fully demonstrating a single-phase reaction mechanism and excellent structural stability. More precisely, the representative (002) peak of P2 phase and another (004) peak consecutively shift leftward in the first de-sodiation process, on the contrary, these (10l) peaks experience a rightward tendency. These observations exhibit that the removal of Na^+ ions bring about enhanced O^{2-}-O^{2-} repulsion effect from adjacent transition metal layers and shrinking of the TMO_6 octahedra, thereby giving rise to the enlargement of the c axis and the contraction of parameter a. Upon Na^+ insertion, this material delivers outstanding reversibility due to the diffraction peaks move toward a converse direction compared with the charging process [46,49,63]. Furthermore, we can find that the (00l) peaks and (10l) peaks are located at higher and lower angles than their original state, respectively, after discharging, suggesting more Na^+ intercalates into the host structure. And the corresponding ex-situ XRD patterns of NCM@5AP cathode behaves the similar tendency (Fig. S18a). In contrast, the pristine

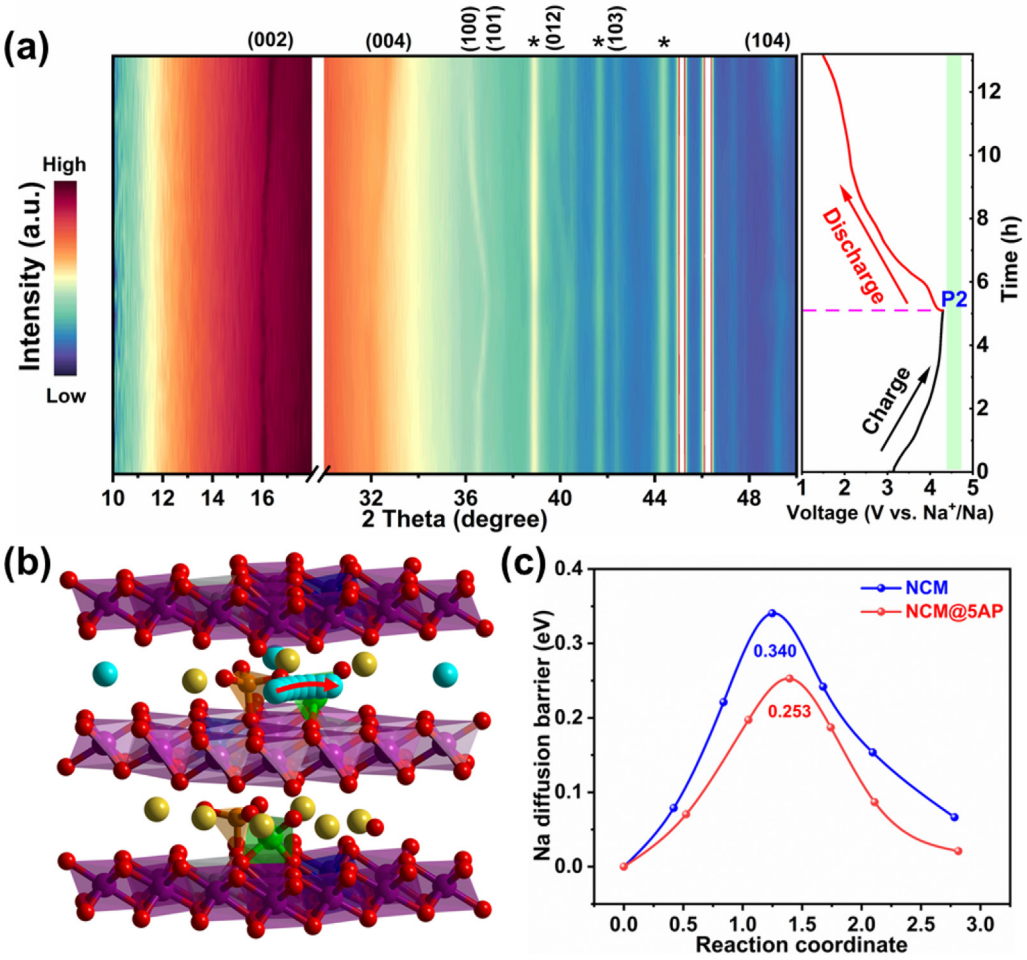

Fig. 5. (a) In-situ XRD patterns collected during the first charge/discharge process of the NCM@5AP electrode between 1.5 and 4.3 V. Black asterisks represent peaks of the Be window. (b) Diffusion path of NCM@5AP cathode simulated by first-principles calculation (Mn: purple, Co: blue, Ni: grey, O: red, Na: yellow and cyan, Al: green, and P: orange). (c) The calculated migration energy barrier of Na^+ in pristine NCM and NCM@5AP electrodes.

NCM electrode undergoes a P2-OP4 phase transition, as revealed by the ex-situ XRD results in Fig. S18(b) [17]. It manifests that the protective AP layer can inhibit the glide of transition metal layers and harmful phase transition, thus realizing stable crystal structure and better electrochemical properties.

DFT was employed to further unravel the reason of the ameliorated electrochemical performance of NCM@5AP cathode after AP modification. The Na^+ diffusion paths and the corresponding calculated migration energy barriers of the pristine NCM and NCM@5AP electrodes are presented in Fig. 5(b–c) and Fig. S19. It is obvious that the energy barrier of NCM@5AP is lower than that of the pristine NCM, corroborating that surface modification can accelerate the diffusion rate of Na^+ ions. To track the cause of dramatical capacity fading of pristine NCM electrode, SEM images of the four as-prepared cathode materials after 100 cycles are illustrated in Fig. S20. Apparently, most of the pristine NCM plates are broken into nanoparticles and the surface of the remaining material becomes rough, suggesting the occurrence of unfavorable phase transition and Jahn-Teller effect of Mn^{3+}. However, the AP-coated electrode materials, especially the NCM@5AP, almost maintain the intact morphology, indicating that the AP coating layer greatly mitigates the aforementioned drawbacks and ameliorate structural stability. Moreover, the pristine NCM shows new hydration phase when exposed to air, while the XRD pattern of NCM@5AP remains stable, revealing that AP greatly improved the air stability of the electrode (Fig. S21) [64].

For the purpose of evaluating the practical application potential of the as-synthesized P2-type cathode, the NCM@5AP electrode was paired with commercial hard carbon as anode material to assemble full batteries. The hard carbon anode exhibits a reversible capacity of approximately 230 mA h g^{-1} at 20 mA g^{-1} (Fig. S22). To maintain capacity balance, the cathode-to-anode ratio was set at 1.4:1 (Fig. S23a). The full cell tested at a rate of 20 mA g^{-1} within the voltage window of 2.0–4.2 V can deliver a reversible capacity of 98 mA h g^{-1} based on the cathode material, and it maintains 80.4% of its initial capacity after 50 cycles. Furthermore, even at a high rate of 500 mA g^{-1}, this cell can still achieve a reversible discharge capacity of 45 mA h g^{-1} (Fig. S23b–d).

4. Conclusions

In conclusion, we successfully synthesized amorphous $AlPO_4$-coated P2-type $Na_{0.55}Ni_{0.1}Co_{0.1}Mn_{0.8}O_2$ cathode materials using a facile solid-state reaction combined with a wet chemical precipitation strategy. The protective coating plays a crucial role in enhancing the electrochemical performance by addressing several key challenges. Firstly, the coating effectively mitigates the Jahn-Teller effect of Mn^{3+} by reducing the amount of Mn^{3+} ions, thereby enhancing the structural stability and prolonging the cycling life of the electrode. Additionally, it inhibits parasitic reactions between the active material and electrolyte, minimizing capacity fading during repeated cycling. Furthermore, the coating layer creates an enlarged interlayer diffusion space for Na^+ ions, facilitating their transfer within the electrode structure. This enhancement in Na^+ diffusion kinetics contributes to the improved rate capacity of the composite electrode. As a result of these beneficial effects, the optimized composite electrode with 5 wt% coating retains an impressive 78.4% of its initial capacity after 200 cycles at 100 mA g^{-1} and exhibits a significantly enhanced rate capacity of 98 mA h g^{-1} even at a high discharge rate of 500 mA g^{-1}. Overall, our facile surface engineering strategy demonstrates a promising approach to enhance the electrochemical properties of layered P2-type Mn-based cathode materials. It opens up new possibilities for practical applications in advanced sodium-ion battery systems.

CRediT authorship contribution statement

Jun Xiao: Writing – review & editing, Writing – original draft, Methodology, Investigation, Formal analysis, Data curation. **Yang Xiao:** Writing – review & editing, Writing – original draft, Investigation, Data curation. **Shijian Wang:** Writing – review & editing, Investigation, Formal analysis, Data curation. **Zefu Huang:** Writing – review & editing, Investigation, Formal analysis, Data curation. **Jiayi Li:** Writing – review & editing, Investigation, Formal analysis. **Cheng Gong:** Writing – review & editing, Formal analysis, Data curation. **Guilai Zhang:** Writing – review & editing, Formal analysis, Data curation. **Bing Sun:** Writing – review & editing, Supervision, Conceptualization. **Hong Gao:** Writing – review & editing, Supervision, Funding acquisition, Conceptualization. **Huiqiao Li:** Funding acquisition, Project administration, Writing – review & editing. **Xin Guo:** Writing – review & editing, Supervision, Formal analysis. **Yong Wang:** Writing – review & editing, Supervision, Resources, Funding acquisition. **Hao Liu:** Writing – review & editing, Writing – original draft, Supervision, Resources, Funding acquisition, Conceptualization. **Guoxiu Wang:** Writing – review & editing, Supervision, Conceptualization.

Declaration of competing interest

The authors declare that they have no known competing financial interests or personal relationships that could have appeared to influence the work reported in this paper.

Acknowledgments

This project is financially supported by the Australian Research Council (ARC) through the Future Fellowship (FT180100705). J.X. thanks the financial support from China Scholarship Council. H.L. and H.L. thank the support from UTS-HUST Key Technology Partner Seed Fund. H.G. and Y.W. thank the support from Open Project of State Key Laboratory of Advanced Special Steel, the Shanghai Key Laboratory of Advanced Ferrometallurgy, Shanghai University (SKLASS 2021-04) and the Science and Technology Commission of Shanghai Municipality (22010500400), "Joint International Laboratory on Environmental and Energy Frontier Materials" and "Innovation Research Team of High–Level Local Universities in Shanghai" in Shanghai University.

Appendix A. Supplementary material

Supplementary data to this article can be found online at https://doi.org/10.1016/j.jechem.2024.06.007.

References

[1] C.L. Zhao, Q.D. Wang, Z.P. Yao, J.L. Wang, B. Sanchez-Lengeling, F.X. Ding, X.G. Qi, Y.X. Lu, X.D. Bai, B.H. Li, H. Li, A. Aspuru-Guzik, X.J. Huang, C. Delmas, M. Wagemaker, L.Q. Chen, Y.S. Hu, Science 370 (2020) 708–711.
[2] Z. Chen, M. Yang, G. Chen, G. Tang, Z. Huang, M. Chu, R. Qi, S. Li, R. Wang, C. Wang, T. Zhang, J. Zhai, W. Zhao, J. Zhang, J. Chen, L. He, J. Xu, W. Yin, J. Wang, Y. Xiao, Nano Energy 94 (2022) 106958.
[3] X.L. Li, T. Wang, Y. Yuan, X.Y. Yue, Q.C. Wang, J.Y. Wang, J. Zhong, R.Q. Lin, Y. Yao, X.J. Wu, X.Q. Yu, Z.W. Fu, Y.Y. Xia, X.Q. Yang, T. Liu, K. Amine, Z. Shadike, Y. N. Zhou, J. Lu, Adv. Mater. 33 (2021) 2008194.
[4] N. Voronina, N. Yaqoob, H.J. Kim, K.S. Lee, H.D. Lim, H.G. Jung, O. Guillon, P. Kaghazchi, S.T. Myung, Adv. Energy Mater. 11 (2021) 2100901.
[5] X. Rong, E. Hu, Y. Lu, F. Meng, C. Zhao, X. Wang, Q. Zhang, X. Yu, L. Gu, Y.-S. Hu, H. Li, X. Huang, X.-Q. Yang, C. Delmas, L. Chen, Joule 3 (2019) 503–517.
[6] J. Chen, G. Zhang, J. Xiao, J. Li, Y. Xiao, D. Zhang, H. Gao, X. Guo, G. Wang, H. Liu, Adv. Funct. Mater. 34 (2024) 2307959.
[7] X.L. Li, J. Bao, Y.F. Li, D. Chen, C. Ma, Q.Q. Qiu, X.Y. Yue, Q.C. Wang, Y.N. Zhou, Adv. Sci. 8 (2021) 2004448.
[8] K. Liu, S. Tan, J. Moon, C.J. Jafta, C. Li, T. Kobayashi, H. Lyu, C.A. Bridges, S. Men, W. Guo, Y. Sun, J. Zhang, M.P. Paranthaman, X.G. Sun, S. Dai, Adv. Energy Mater. 10 (2020) 2000135.

[9] L. Zhang, J. Wang, G. Schuck, F. Xi, L. Du, M. Winter, G. Schumacher, J. Li, Small Methods 4 (2020) 2000422.
[10] X. Cao, H. Li, Y. Qiao, X. Li, M. Jia, J. Cabana, H. Zhou, Adv. Energy Mater. 10 (2020) 1903785.
[11] R.A. House, U. Maitra, M.A. Perez-Osorio, J.G. Lozano, L. Jin, J.W. Somerville, L.C. Duda, A. Nag, A. Walters, K.J. Zhou, M.R. Roberts, P.G. Bruce, Nature 577 (2020) 502–508.
[12] B. Xiao, X. Liu, X. Chen, G.H. Lee, M. Song, X. Yang, F. Omenya, D.M. Reed, V. Sprenkle, Y. Ren, C.J. Sun, W. Yang, K. Amine, X. Li, G. Xu, X. Li, Adv. Mater. 33 (2021) 2107141.
[13] Y. Xiao, J. Xiao, H. Zhao, J. Li, G. Zhang, D. Zhang, X. Guo, H. Gao, Y. Wang, J. Chen, G. Wang, H. Liu, Small (2024). https://doi.org/10.1002/smll.202401957.
[14] Q. Mao, R. Gao, Q. Li, D. Ning, D. Zhou, G. Schuck, G. Schumacher, Y. Hao, X. Liu, Chem. Eng. J. 382 (2020) 122978.
[15] J. Xiao, Y. Xiao, J. Li, C. Gong, X. Nie, H. Gao, B. Sun, H. Liu, G. Wang, SmartMat 4 (2023) e1211.
[16] Y. Wang, K. Tang, X. Li, R. Yu, X. Zhang, Y. Huang, G. Chen, S. Jamil, S. Cao, X. Xie, Z. Luo, X. Wang, Chem. Eng. J. 372 (2019) 1066–1076.
[17] J.Y. Hwang, J. Kim, T.Y. Yu, Y.K. Sun, Adv. Energy Mater. 9 (2019) 1803346.
[18] H. Liu, X. Liu, W. Li, X. Guo, Y. Wang, G. Wang, D. Zhao, Adv. Energy Mater. 7 (2017) 1700283.
[19] J.H. Jo, J.U. Choi, A. Konarov, H. Yashiro, S. Yuan, L. Shi, Y.K. Sun, S.T. Myung, Adv. Funct. Mater. 28 (2018) 1705968.
[20] J. Song, K. Wang, J. Zheng, M.H. Engelhard, B. Xiao, E. Hu, Z. Zhu, C. Wang, M. Sui, Y. Lin, D. Reed, V.L. Sprenkle, P. Yan, X. Li, ACS Energy Lett. 5 (2020) 1718–1725.
[21] Y. Xiao, P.F. Wang, Y.X. Yin, Y.F. Zhu, Y.B. Niu, X.D. Zhang, J. Zhang, X. Yu, X.D. Guo, B.H. Zhong, Y.G. Guo, Adv. Mater. 30 (2018) 1803765.
[22] Y.F. Zhu, Y. Xiao, W.B. Hua, S. Indris, S.X. Dou, Y.G. Guo, S.L. Chou, Angew. Chem., Int. Ed. 59 (2020) 9299–9304.
[23] S.Y. Zhang, Y.J. Guo, Y.N. Zhou, X.D. Zhang, Y.B. Niu, E.H. Wang, L.B. Huang, P.F. An, J. Zhang, X.A. Yang, Y.X. Yin, S. Xu, Y.G. Guo, Small 17 (2021) 2007236.
[24] H. Gao, J. Li, F. Zhang, C. Li, J. Xiao, X. Nie, G. Zhang, Y. Xiao, D. Zhang, X. Guo, Y. Wang, Y.M. Kang, G. Wang, H. Liu, Adv. Energy Mater. 14 (2024) 2304529.
[25] Q.C. Wang, J.K. Meng, X.Y. Yue, Q.Q. Qiu, Y. Song, X.J. Wu, Z.W. Fu, Y.Y. Xia, Z. Shadike, J. Wu, X.Q. Yang, Y.N. Zhou, J. Am. Chem. Soc. 141 (2019) 840–848.
[26] C. Wang, L. Liu, S. Zhao, Y. Liu, Y. Yang, H. Yu, S. Lee, G.H. Lee, Y.M. Kang, R. Liu, F. Li, J. Chen, Nat. Commun. 12 (2021) 2256.
[27] N. Jiang, Q. Liu, J. Wang, W. Yang, W. Ma, L. Zhang, Z. Peng, Z. Zhang, Small 17 (2021) 2007103.
[28] J. Xu, Z. Han, K. Jiang, P. Bai, Y. Liang, X. Zhang, P. Wang, S. Guo, H. Zhou, Small 16 (2020) 1904388.
[29] L. Yang, L.Y. Kuo, J.M. López del Amo, P.K. Nayak, K.A. Mazzio, S. Maletti, D. Mikhailova, L. Giebeler, P. Kaghazchi, T. Rojo, P. Adelhelm, Adv. Funct. Mater. 31 (2021) 2102939.
[30] J. Xiao, X. Li, K. Tang, D. Wang, M. Long, H. Gao, W. Chen, C. Liu, H. Liu, G. Wang, Mater. Chem. Front. 5 (2021) 3735–3764.
[31] L. Yang, X. Li, J. Liu, S. Xiong, X. Ma, P. Liu, J. Bai, W. Xu, Y. Tang, Y.Y. Hu, M. Liu, H. Chen, J. Am. Chem. Soc. 141 (2019) 6680–6689.
[32] Y. Xie, E. Gabriel, L. Fan, I. Hwang, X. Li, H. Zhu, Y. Ren, C. Sun, J. Pipkin, M. Dustin, M. Li, Z. Chen, E. Lee, H. Xiong, Chem. Mater. 33 (2021) 4445–4455.
[33] Y. Wang, L. Wang, H. Zhu, J. Chu, Y. Fang, L. Wu, L. Huang, Y. Ren, C.J. Sun, Q. Liu, X. Ai, H. Yang, Y. Cao, Adv. Funct. Mater. 30 (2020) 1910327.
[34] L. Yang, S.-H. Luo, Y. Wang, Y. Zhan, Q. Wang, Y. Zhang, X. Liu, W. Mu, F. Teng, Chem. Eng. J. 404 (2021) 126578.
[35] T. Chen, W. Liu, Y. Zhuo, H. Hu, M. Zhu, R. Cai, X. Chen, J. Yan, K. Liu, J. Energy Chem. 43 (2020) 148–154.
[36] C. Zhao, Z. Yao, J. Wang, Y. Lu, X. Bai, A. Aspuru-Guzik, L. Chen, Y.-S. Hu, Chem 5 (2019) 2913–2925.
[37] L. Yang, J.M.L. Amo, Z. Shadike, S.M. Bak, F. Bonilla, M. Galceran, P.K. Nayak, J.R. Buchheim, X.Q. Yang, T. Rojo, P. Adelhelm, Adv. Funct. Mater. 30 (2020) 2003364.
[38] Z. Yan, L. Tang, Y. Huang, W. Hua, Y. Wang, R. Liu, Q. Gu, S. Indris, S.L. Chou, Y. Huang, M. Wu, S.X. Dou, Angew. Chem., Int. Ed. 58 (2019) 1412–1416.
[39] Y.-N. Zhou, P.-F. Wang, Y.-B. Niu, Q. Li, X. Yu, Y.-X. Yin, S. Xu, Y.-G. Guo, Nano Energy 55 (2019) 143–150.
[40] C. Sun, S. Li, M. Bai, W. Wu, X. Tang, W. Zhao, M. Zhang, Y. Ma, Energy Storage Mater. 27 (2020) 252–260.
[41] B. Hu, F. Geng, C. Zhao, B. Doumert, J. Trebosc, O. Lafon, C. Li, M. Shen, B. Hu, ACS Appl. Mater. Interfaces 12 (2020) 41485–41494.
[42] C.H. Jo, J.H. Jo, H. Yashiro, S.J. Kim, Y.K. Sun, S.T. Myung, Adv. Energy Mater. 8 (2018) 1702942.
[43] Y. Zhang, Y. Pei, W. Liu, S. Zhang, J. Xie, J. Xia, S. Nie, L. Liu, X. Wang, Chem. Eng. J. 382 (2020) 122697.
[44] Y. Li, Q. Shi, X. Yin, J. Wang, J. Wang, Y. Zhao, J. Zhang, Chem. Eng. J. 402 (2020) 126181.
[45] Q. Deng, F. Zheng, W. Zhong, Q. Pan, Y. Liu, Y. Li, Y. Li, J. Hu, C. Yang, M. Liu, Chem. Eng. J. 404 (2021) 126446.
[46] Y. Xiao, Y.F. Zhu, H.R. Yao, P.F. Wang, X.D. Zhang, H. Li, X. Yang, L. Gu, Y.C. Li, T. Wang, Y.X. Yin, X.D. Guo, B.H. Zhong, Y.G. Guo, Adv. Energy Mater. 9 (2019) 1803978.
[47] J. Xiao, F. Zhang, K. Tang, X. Li, D. Wang, Y. Wang, H. Liu, M. Wu, G. Wang, ACS Cent. Sci. 5 (2019) 1937–1945.
[48] J.U. Choi, J.H. Jo, Y.J. Park, K.S. Lee, S.T. Myung, Adv. Energy Mater. 10 (2020) 2001346.
[49] Y. Liu, Q. Shen, X. Zhao, J. Zhang, X. Liu, T. Wang, N. Zhang, L. Jiao, J. Chen, L.Z. Fan, Adv. Funct. Mater. 30 (2019) 1907837.
[50] K. Kaliyappan, W. Xaio, T.K. Sham, X. Sun, Adv. Funct. Mater. 28 (2018) 1801898.
[51] B. Peng, Z. Sun, L. Zhao, J. Li, G. Zhang, Energy Storage Mater. 35 (2021) 620–629.
[52] T. Fang, S. Guo, K. Jiang, X. Zhang, D. Wang, Y. Feng, X. Zhang, P. Wang, P. He, H. Zhou, Small Methods 3 (2018) 1800183.
[53] Q.C. Wang, Z. Shadike, X.L. Li, J. Bao, Q.Q. Qiu, E. Hu, S.M. Bak, X. Xiao, L. Ma, X.J. Wu, X.Q. Yang, Y.N. Zhou, Adv. Energy Mater. 11 (2021) 2003455.
[54] Y. Zhang, M. Wu, J. Ma, G. Wei, Y. Ling, R. Zhang, Y. Huang, ACS Cent. Sci. 6 (2020) 232–240.
[55] J.E. Wang, H. Kim, Y.H. Jung, D.K. Kim, D.J. Kim, Small 17 (2021) 2100146.
[56] Q. Huang, J. Liu, L. Zhang, S. Xu, L. Chen, P. Wang, D.G. Ivey, W. Wei, Nano Energy 44 (2018) 336–344.
[57] J. Lamb, L. Stokes, A. Manthiram, Chem. Mater. 32 (2020) 7389–7396.
[58] Q. Zhang, Z. Wang, X. Li, H. Guo, W. Peng, J. Wang, G. Yan, Chem. Eng. J. 431 (2022) 133456.
[59] H. Li, T. Wang, X. Wang, G. Li, Y. Du, J. Shen, J. Chai, J. Power Sources 494 (2021) 229771.
[60] N.Q. Quyen, T. Van Nguyen, H.H. Thang, P.M. Thao, N. Van Nghia, J. Alloys Compd. 866 (2021) 158950.
[61] Y. Liu, J. Yang, B. Guo, X. Han, Q. Yuan, Q. Fu, H. Lin, G. Liu, M. Xu, Nanoscale 10 (2018) 12625–12630.
[62] J. Xiao, H. Gao, K. Tang, M. Long, J. Chen, H. Liu, G. Wang, Small Methods 6 (2022) 2101292.
[63] Q. Shen, X. Zhao, Y. Liu, Y. Li, J. Zhang, N. Zhang, C. Yang, J. Chen, Adv. Sci. 7 (2020) 2002199.
[64] W. Zuo, J. Qiu, X. Liu, F. Ren, H. Liu, H. He, C. Luo, J. Li, G.F. Ortiz, H. Duan, J. Liu, M.S. Wang, Y. Li, R. Fu, Y. Yang, Nat. Commun. 11 (2020) 3544.